

# Investigations of heat extraction for water and CO<sub>2</sub> flow based on the rough-walled discrete fracture network

Jiawei Li <sup>a</sup>, Zhixue Sun <sup>b,\*</sup>, Yin Zhang <sup>c</sup>, Chuanyin Jiang <sup>b</sup>, Claudia Cherubini <sup>d</sup>,  
Alexander Scheuermann <sup>a</sup>, Sergio Andres Galindo Torres <sup>e</sup>, Ling Li <sup>e,\*\*</sup>

<sup>a</sup> School of Civil Engineering, University of Queensland, Brisbane, 4072, Australia

<sup>b</sup> School of Petroleum Engineering, China University of Petroleum (East China), Qingdao, 266580, China

<sup>c</sup> College of Engineering and Mines, University of Alaska Fairbanks, Fairbanks, 755960, United States

<sup>d</sup> Department of Physics and Earth Sciences, University of Ferrara, Via Saragat 1, 44122, Ferrara, Italy

<sup>e</sup> School of Engineering, Westlake University, Hangzhou, 310024, China

## ARTICLE INFO

### Keywords:

Rough fractures  
Discrete fracture network  
Thermal-hydraulic-mechanical coupling  
Heat extraction

## ABSTRACT

The Enhanced Geothermal Systems (EGS) has been developed to enhance geothermal energy extraction efficiency from geothermal reservoirs by generating effective fracture network. The fracture effective network that are comprised by rough-walled fractures can provide a more realistic reflection of natural reservoir conditions. This study focuses on the construction of a rough-walled discrete fracture model to simulate mass and heat transfer in a geothermal reservoir by using water and CO<sub>2</sub> as the working fluid. The thermal-hydraulic-mechanical (THM) coupling process was integrated into the rough-walled discrete fracture network model. The heat mining processes with two working fluids (water and CO<sub>2</sub>) were simulated with the parallel-plate and rough-walled discrete fracture network models. The influences of the parallel and rough-walled discrete fracture network models on flow behaviours, heat transfer and corresponding mechanical responses for water and CO<sub>2</sub> were presented and analysed. What's more, the heat extraction efficiency based on the combination of rough-walled discrete fracture network and the THM method were calculated and analysed in details. The influences of pressure, temperature, fluids and reservoir rock properties on heat extraction rates were also considered.

It is found that CO<sub>2</sub> leads to faster pressure changes compared with water in both parallel-plate and rough-walled discrete fracture network models. The influences of the pressure and temperature distributions on the permeability and normal stress were also evaluated, which contribute to the investigation of the deforming mechanisms of the rock matrix and fractures. In addition, there are certain differences in the heat production rate between the parallel-plate and rough-walled discrete fracture networks, which reflects that the rough-walled discrete fracture network used in this study has a better conductivity. It is also found that water can be a more efficient working fluid for heat extraction from geothermal reservoirs compared with CO<sub>2</sub> during certain production durations in this study. The results of this study present that the rough-walled discrete network model has a great significance in the simulation of the real conditions and processes in geothermal reservoirs during the heat mining process.

## 1. Introduction

In recent years, the exploitation and production of geothermal energy resources, including natural hydrothermal resources and

Hot Dry rock (HDR), play an increasing role in energy supply and environmental protection for the world [1–3]. The total geothermal capacity has reached about 18.4 GW in 2018 [4,5]. The geothermal energy extraction can be directly produced from natural hydrothermal resources with sufficient reservoir permeabilities. Investigations show that the majority of geothermal resources is stored at deeper subsurface that are almost impermeable with little fluids [6,7]. In order to extract geothermal energy from deep geothermal reservoirs, the Enhanced Geothermal Systems (EGS)

\* Corresponding author.

\*\* Corresponding author.

E-mail addresses: [jiawei.li@uq.edu.au](mailto:jiawei.li@uq.edu.au) (J. Li), [upcszx@upc.edu.cn](mailto:upcszx@upc.edu.cn) (Z. Sun), [liling@westlake.edu.cn](mailto:liling@westlake.edu.cn) (L. Li).

technologies have been developed by using working fluids (water and CO<sub>2</sub>) [8–10]. With the injection of working fluids, the fracture networks in geothermal reservoirs are generated that produce economic production flow rates [11]. EGS has attracted more and more attentions because it can enhance geothermal play system conditions from non-economic to economic conditions [12].

Since 2010, many approaches for modelling geothermal reservoirs have been proposed and developed to investigate performances of EGS [13–16]. Shaik et al. [17] has developed a model that couples fluid flow with heat transfer based on a discrete fracture network model with purpose of evaluating heat extraction efficiency from fractured geothermal reservoirs. The dual-porosity multiple interacting continua model has been used to simulate salt precipitation process and its effects on production rates with the injection of CO<sub>2</sub> as the working fluid [18]. A three dimensional transient model that integrates thermal-hydraulic process during the heat mining has been presented with taking different characteristic properties for multiple subregions in the whole reservoir [19]. In addition to numerical models, an analytical model for a two dimensional discrete fracture network to simulate fluid flow and heat transfer in geothermal reservoirs has been proposed and validated [20]. Sun et al. [21] have built a numerical model based on the discrete fracture network to simulate the thermal-hydraulic-mechanical (THM) coupling effects on heat extraction during the heat mining process. Fractures that are induced by the injection of CO<sub>2</sub> in geothermal reservoirs have been given an accurate characterization by analysing geophysical responses [22]. The heat extraction performance for EGS in heterogeneous reservoirs has been quantified by analysing fluid seepage flow in a single porosity system [23]. And it is found that the heat extraction efficiency flow distribution in a discrete fracture network during the heat mining process depends on the amount of fractures in the reservoir [24].

With the purpose of easier quantification and lower computational cost, fractures in models have been assumed to be parallel plates in most cases [25–28]. However, the fact that natural fracture surfaces are rough cannot be ignored. To date, the studies on fluids flow through a single rough fracture and rough fractures network have been pretty limited. The non-Darcy flow behaviours through a single rough fracture and relevant impacting factors (boundary condition, fracture roughness, etc.) have been simulated and analysed [29]. The influences of wettability on interfacial areas through a single rough fractures have also been discussed and evaluated based on Lattice Boltzmann simulations [30]. The model for fluid flow through two intersected rough fractures has been simulated and corresponding channel flow patterns have been found [31]. Dreuzy et al. [32] have investigated the effects of single fracture aperture heterogeneity on flow behaviours in a 3D discrete fracture network, where the roughness of fracture surfaces results in aperture heterogeneity. A discrete rough-fracture network model at the core scale has been developed to simulate gas flow in coal seam gas reservoirs, finding that the new model can provide a more accurate permeability estimation compared with the older ones [33]. A rough-walled discrete fracture model has been applied for the simulation of fluids flow and heat transfer in geothermal reservoirs by simplifying the fractures and matrix [34]. The model of a single rough fracture between production and injection wells in the geothermal reservoir has been proposed and simulated [35–37].

During the process of mathematical modelling, the effects of rock matrix on fluid flow are negligible due to the fact that the reservoir rock is almost impermeable. In this paper, the properties of rough fractures are characterized and a rough-walled discrete network model is built to simulate fluid flow and heat transfer in geothermal reservoirs with the injection of both water and CO<sub>2</sub>. The THM process are integrated into the rough-walled discrete fracture

network model because the THM process allow a more realistic reflection for the simulation of EGS.

## 2. Single rough fracture and fracture networks in three dimensional space

The rough surfaces of fractures have been found to meet the distributions of self-affine fractal geometry [38,39]. In fractal geometry, a parameter, fractal dimension  $D$ , is proposed to as a statistical index of the complexity in a fractal pattern corresponding to measured scale. The range of the fractal dimension for the two dimensional space distributes between 1 and 2 and it mostly locates in the range of 1 and 1.5 for rough surfaces of natural fractures [40]. In three dimensional space, the range of the fractal dimension is from 2 to 3 and it is typically from 2.15 to 2.55 in most cases. The fracture surfaces are smoother when the fractal dimension is closer to 1 in two dimensional space and 2 in three dimensional space respectively.

In this study, the fractal dimension in three-dimensional space is used as examples. The correlation between the fractal dimension and Hurst exponent  $H$  can be expressed as the following equation:

$$D = 3 - H \quad (1)$$

where  $D$  is the fractal dimension,  $H$  is the Hurst exponent, another parameter for fracture surface quantification.

In mathematical modelling, the roughness of single fracture surfaces are characterized by the heterogeneous aperture distributions of the single fracture. Fig. 1 shows that the bottom surfaces of three dimensional fractures corresponds to different values of the fractal dimension with other parameters being constant. The size of the fracture bottom surface is  $12.8 \times 12.8$  cm along X and Y directions and  $64 \times 64$  sets of heights along Z directions exist on the surface. It can be found that the height distributions show a gradual change with the increasing values of the fractal dimension. The top and bottom surfaces of a fracture is shown in Fig. 2. In addition, the corresponding statistical histogram follows a Gaussian distribution.

In the geothermal reservoir with the realistic condition, a rough-walled discrete fracture network is made up by single rough fractures distributed in various locations of the three dimensional (3D) space. The generation of rough-walled discrete fracture network is based on the method proposed by Lei et al [41]. Fig. 3 shows an example of a simple schematic of 3D rough-walled discrete fracture network. It can be seen that single rough fractures are interconnected with close ones. The aperture heterogeneities of single rough fractures are also reflected: different colours of the colour bar represent different values of apertures, varying from 0 to  $2.5 \times 10^{-5}$  mm.

## 3. Model description

As is shown in Figs. 2 and 3, an accurate reflection of rough fractures in 3D space requires a large number of grids that should be small enough and calculations in 3D space generate highly computational loads. In order to enhance computational efficiency, 2D discrete fracture networks are adopted to study the performance of heat and mass transfer for water and CO<sub>2</sub> flow in the geothermal reservoir during the process of EGS. Fig. 4 is a simple 2D schematic of the EGS with water as the working fluid. In this study, one vertical injection well and one vertical production well are considered as is shown in Fig. 4.

In this study, the mathematical model is developed on the basis of the following assumptions:

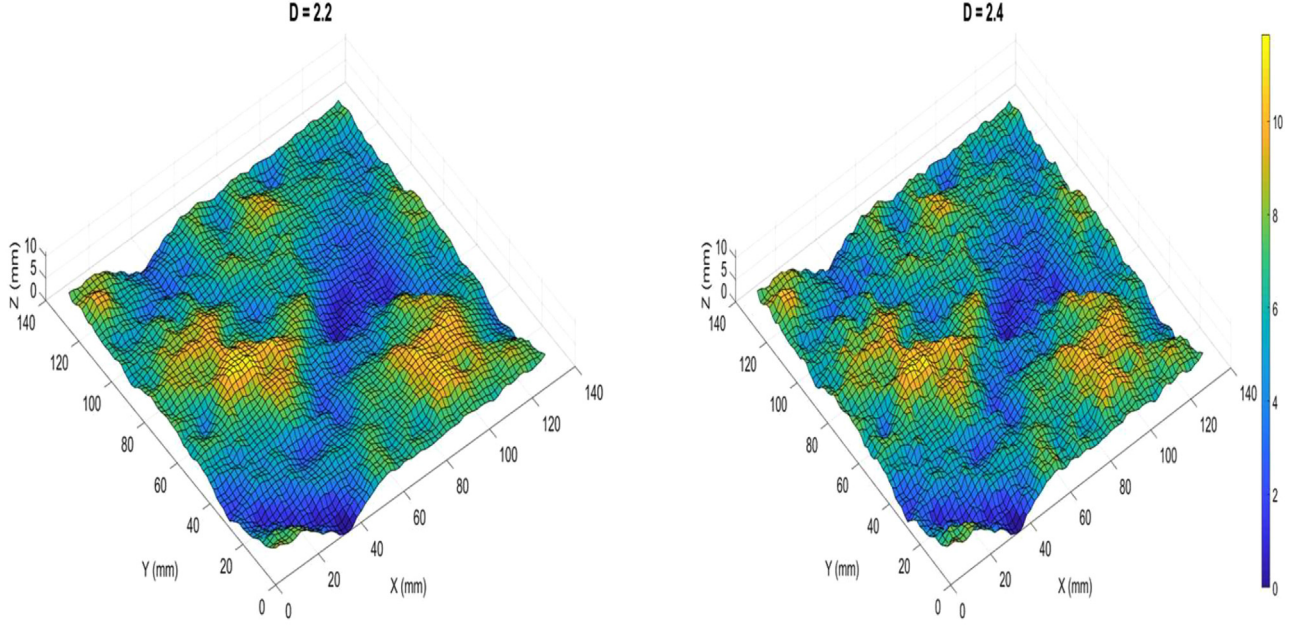


Fig. 1. Two bottom surfaces for the fractal dimension  $D = 2.2$  and  $2.4$ .

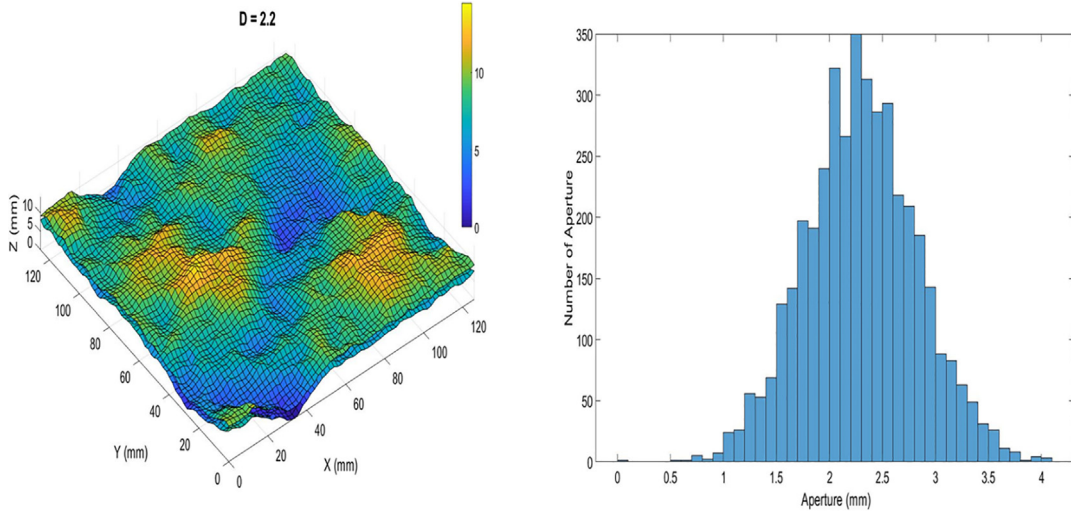


Fig. 2. Top and bottom surfaces of a fracture and corresponding statistical histogram for the fractal dimension  $D = 2.2$ .

- i) The reservoir model is a dual porosity system that includes rock matrix and discrete fracture network. The rock matrix is isotropic and its permeability is much lower than the permeability of fractures.
- ii) The deformation of rock mass is thermal- and pressure-dependent.
- iii) In the reservoir, the water and  $\text{CO}_2$  flow are liquid and liquid-like states, following Darcy Law.
- iv) Only heat conduction and convection process happen during the process of EGS.
- v) The fluids that exist in the reservoir originally is same as the working fluid.

The mass and energy balance equations for single phase flow (water/ $\text{CO}_2$ ) through rock matrix and fractures in the geothermal reservoir can be written as [42–44]:

In the rock matrix:

$$S_m \frac{\partial p}{\partial t} + \nabla \cdot \mathbf{u}_m = -\frac{\partial e_m}{\partial t} \quad (2)$$

$$\phi \rho_i C_i \frac{\partial T_i}{\partial t} + \rho_i C_i \cdot \mathbf{u}_m \nabla T_i = \phi \lambda_i \nabla^2 T_i \quad (3)$$

$$\mathbf{u}_m = -\frac{k_m}{\mu_i} (\nabla p + \rho_i g \nabla z) \quad (4)$$

In the fracture:

$$d_f S_f \frac{\partial p}{\partial t} + \nabla_\tau \cdot \mathbf{u}_f = d_f \frac{\partial e_f}{\partial t} + Q_f \quad (5)$$

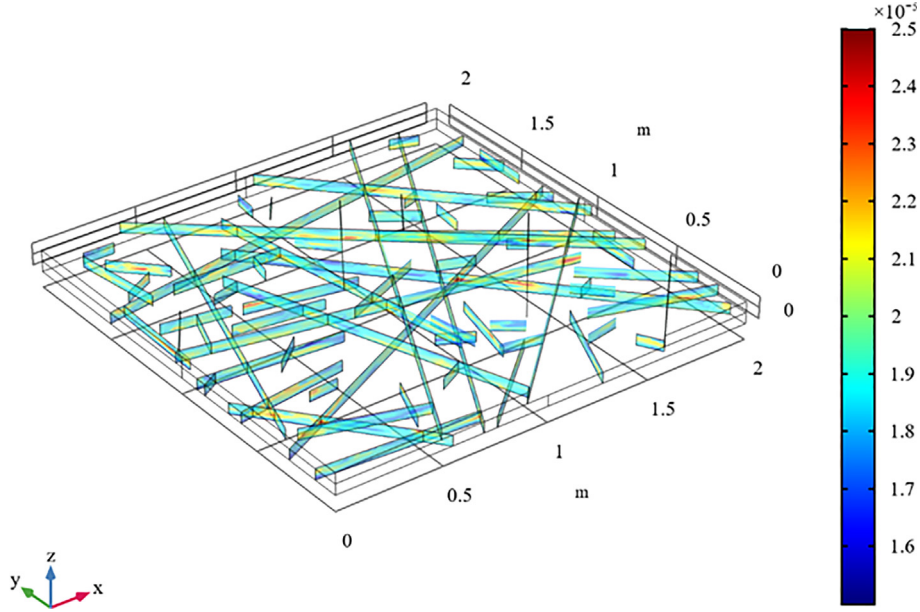


Fig. 3. Schematic of 3D rough-walled discrete fracture network.

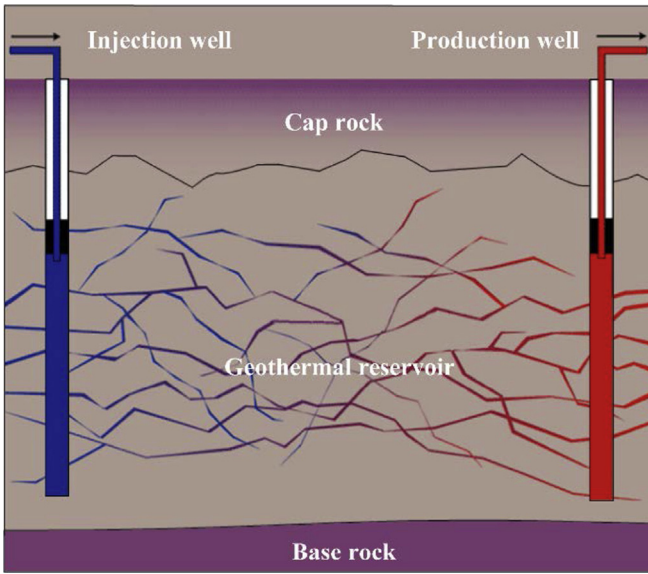


Fig. 4. 2D schematic of the EGS [21].

represents mass transfer between the rock matrix and fracture,  $h$  represents the convection heat transfer coefficient,  $i$  represents fluid flow (water or  $\text{CO}_2$ ).

As is mentioned in the assumptions, the permeability of the rock matrix is much lower than that of the fractures, meaning that the velocity of fluid flow in rock matrix is much lower than the velocity fractures. Thus, it can be considered that the temperature of the fluids in rock matrix is same as the temperature of reservoir rock. The governing equation that describes the heat transfer between the reservoir rock and fluids flow can be expressed as:

$$((1 - \phi)\rho_m C_m + \phi\rho_i C_i) \frac{\partial T_m}{\partial t} = ((1 - \phi)\lambda_m + \phi\lambda_i) \nabla^2 T_m \quad (8)$$

#### 4. Numerical simulation

In Fig. 5, two discrete fracture networks constituted by parallel-plate and rough-walled fractures separately are presented with the scale  $100 \text{ m} \times 100 \text{ m}$  on the  $X \times Y$  plane. The effective length of  $Z$  axis is 1 m. The simulations are realized with the application of the COMSOL Multiphysics, a commercial software based on the finite element method. As is shown in Fig. 5, the reservoir depth that is used for simulation in this study is assumed to be located from 6400 to 6500 m. As for the rough-walled discrete fracture network, the aperture distributions for one fracture is heterogeneous, as is shown in Figs. 2 and 3 by using different colours. The values of fracture apertures are in the range  $1.02 \times 10^{-5} \sim 1.33 \times 10^{-5} \text{ mm}$ . For example, 'a' is a fracture that goes through the whole area in both parallel-plate and rough-walled discrete fracture networks. The colour of the fracture 'a' in the parallel-plate discrete fracture network is pure blue, meaning that the aperture distributions of 'a' is homogenous, however, different colours appear in 'a', which reflect a heterogeneous aperture distributions. The apertures of fractures in the parallel-plate discrete fracture network are set as a constant value that equals to  $1.1237 \times 10^{-5} \text{ mm}$ , which equals to the average aperture of all fractures in the rough-walled discrete fracture network. The other parameters of the parallel-plate and rough-walled discrete fracture networks are same. The

$$d_f \rho_i C_i \frac{\partial T_i}{\partial t} + d_f \rho_i C_i \cdot u_f \nabla_\tau T_i = \nabla_\tau \cdot (d_f \lambda_i \nabla_\tau T_i) + h(T_m - T_f) \quad (6)$$

$$u_f = -d_f \frac{k_f}{\mu_i} (\nabla_\tau p + \rho_i g \nabla_\tau z) \quad (7)$$

where  $m$  represents the rock matrix,  $f$  represents the fracture,  $S$  represents the storage coefficient,  $u$  represents the flow rate,  $e$  represents the volumetric strain,  $d_f$  represents the fracture thickness,  $T$  represent the temperature,  $C$  represents the specific heat conductivity,  $\lambda$  represents the heat conductivity,  $k$  represent the permeability,  $\mu$  represents the fluid viscosity,  $g$  represents the gravity acceleration,  $p$  represents the pressure,  $t$  represents the time,  $z$  is a unit vector,  $\phi$  represents the rock matrix porosity,  $Q$

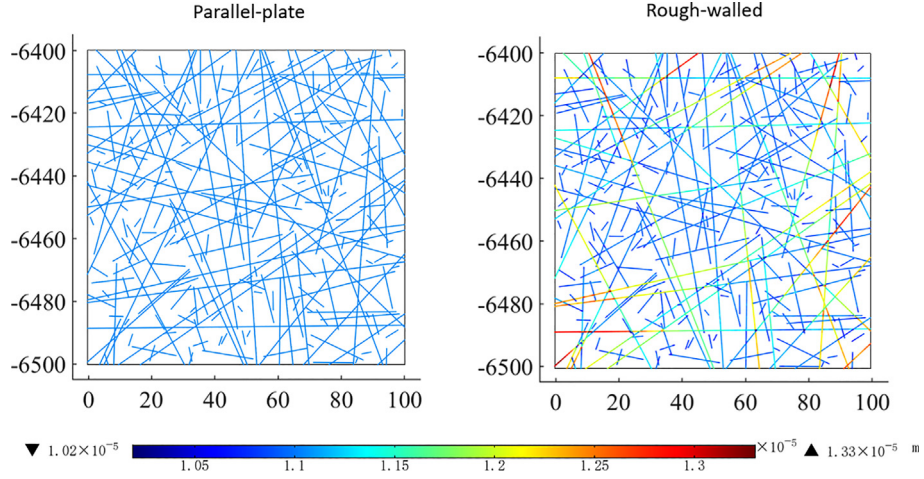


Fig. 5. 2D discrete fracture networks for two different fracture types: parallel-plate and rough-walled.

comparisons of simulation results between the parallel-plate and rough-walled discrete fracture network models can play complementary roles in providing better illustrations and mutual validations of the simulation results.

In this study, water and CO<sub>2</sub> are used as the working fluids for geothermal energy extraction. With the injection and production of working fluids, gradual changes will happen in the pressure and temperature distributions of the whole reservoir. The fact that the properties of fluids are affected by pressure and temperature should be taken into consideration. The density and viscosity of water can be calculated with pressure and temperature [45,46]. Compared with water, CO<sub>2</sub> properties are dependent on pressure and temperature to a much larger extent, the density and viscosity of CO<sub>2</sub> can be calculated based on CMG Winprop [47]. The heat capacities of water and CO<sub>2</sub> are generally temperature dependent and corresponding values of heat capacity can be generated from empirical correlations [48–50]. The thermal conductivities of water and CO<sub>2</sub> are both set as 0 because water and CO<sub>2</sub> as working fluids are not static during the mining process.

The pressure and temperature distributions at initial reservoir conditions are shown in Fig. 6. In Fig. 6-a, the pressure distribution become larger with the increase of the reservoir depth and the initial reservoir pressure is set as 76.93 MPa without considering the gravity effect. In Fig. 6-b, the initial temperature distributions are assumed to be constant, which equals to 200°C. The left and right boundary of the area correspond to the injection and

production wells that are shown in Fig. 4 separately. The given pressure boundary on the left side is set as 78.4 MPa at the reservoir depth 6400 m and the given pressure boundary on the right side equals to 76.44 MPa at the same depth. The top and bottom boundary of this area are assumed to be non-flow boundaries. In addition, the investigated area is thermally confined, which means no heat exchange with the outside. At initial reservoir conditions (high pressure and temperature conditions), there is already stress on the reservoir rock to a certain extent. With taking the fact that the corresponding changes of stress on the reservoir rock that are induced by the working fluids during the heat mining process are the main objective for researchers, the stress on the reservoir rock at initial reservoir conditions can be considered as the standards reference that is set as 0.

The fundamental parameters for reservoir simulations in this study are presented in Table .1. Water and CO<sub>2</sub> are adopted as the working fluids to inject into the reservoir. The injecting temperature of the working fluids is set as 20°C. When the temperature equals to 20°C under the given pressure boundary on the left side, CO<sub>2</sub> stays at the liquid state. After CO<sub>2</sub> are injected into the reservoir, it will transfer into the supercritical state. The phase transitions of CO<sub>2</sub> during the heat mining process are taken into consideration. Compared with CO<sub>2</sub>, the properties of water are much more stable and water always stays at the liquid state. The maximum duration of simulation time in this study is 30 years.

There are two parameters that are needed for a better analysis in

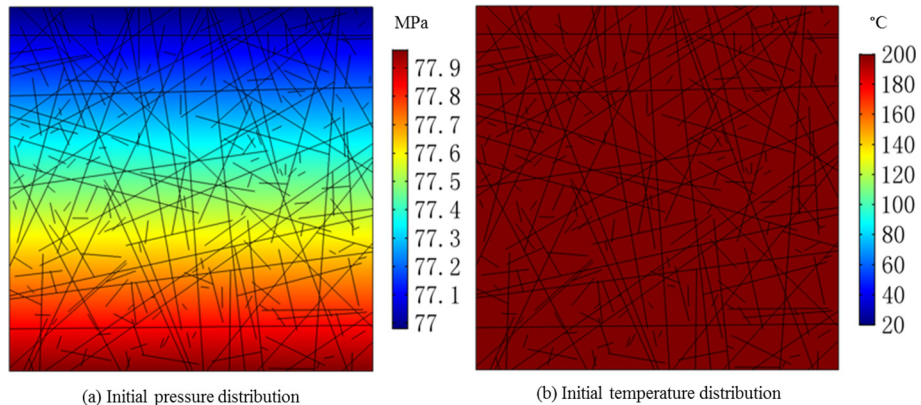


Fig. 6. Initial pressure and temperature distributions in the reservoir.

**Table 1**  
Simulation parameters.

Parameters	Value
Water thermal conductivity $\lambda_{fw}$ , W/m/K	0
CO <sub>2</sub> thermal conductivity $\lambda_{fCO_2}$ , W/m/K	0
Rock density $\rho_{rock}$ , kg/m <sup>3</sup>	2700
Rock heat capacity $C_s$ , J/kg/K	1000
Rock thermal conductivity $\lambda_{rock}$ , W/m/K	3
Rock matrix porosity $\phi$	0.0001
Rock matrix permeability $k_m$ , m <sup>2</sup>	$1.0 \times 10^{-18}$
Convection heat transfer coefficient $h$ , W/m <sup>2</sup> /K	3000
Gravity acceleration $g$ , m/s <sup>2</sup>	9.8
Elastic modulus $E$ , GPa	30
Poisson ratio $\eta$	0.25
Thermal expansion coefficient $\alpha_T$ , K <sup>-1</sup>	$1.0 \times 10^6$
Biot's constant $\alpha_B$	1
Normal stiffness $k_n$ , GPa/m	1200
Tangential stiffness $k_T$ , GPa/m	400
Matrix storage coefficient $S_m$ , 1/Pa	$1.0 \times 10^{-8}$
Fracture storage coefficient $S_f$ , 1/Pa	$1.0 \times 10^{-9}$

this study: the average outlet temperature and the heat extraction rate. The average outlet temperature is calculated with the following equation:

$$T_{out} = \frac{\sum u_f d_f T_f + \int u_m T_m dy}{\sum u_f d_f + \int u_m dy} \quad (9)$$

The heat extraction rate is the differences of the product of the mass flow rate, the absolute value of the temperature decrease and the heat capacity of the working fluid between the injection and production sides, which is expressed in the following equation:

$$G_i = \int_{20}^{T_{out}} (F_i C_i)_{production} - (F_i C_i)_{injection} dT \quad (10)$$

where  $F$  is the mass flow rate.

## 5. Analysis of the results

In Figs. 7 and 8, CO<sub>2</sub> as the working fluid is used to investigate the pressure and temperature distributions changing with time though there are two working fluids (water and CO<sub>2</sub>) that are adopted in this study. Four different time points: 1, 5, 15 and 30 years are chosen. In Fig. 7, it can be seen that the pressure distributions show a decreasing trend from the left side to the right side with corresponding to the locations of the injection and production wells. The gravity effects can be observed that the pressure become larger with the increase of depth. For example, the colour that represents the pressure on the bottom of the left side is deeper in the range of colour 'red' than the colour that represents the pressure on the top of the left side. It can also be found that the pressure changes more rapidly in the area near the fractures due to the large differences of permeability between the rock matrix and fractures. But with time going by, the pressure distributions of the rock matrix and fractures in the close regions tend to be same. In addition, little differences of pressure distributions exist between simulation times 15 and 30 years. As a conclusion, the pressure distribution can be considered to reach the steady state after 15 years.

Fig. 8 illustrates the temperature distributions with time going by in the reservoir. In Fig. 8-a, on the left side, the temperature decreases due the constant injection of CO<sub>2</sub> and the temperature on the right side remains 200°C. In Fig. 8-b, the area of lower

temperature increases because of the ongoing process. The temperature displacement shows an irregular interface because the fracture permeabilities are various. The temperature distributions in Fig. 8-d is the same as the injecting temperature. The distribution of velocity vectors that CO<sub>2</sub> is injected into the rough-walled discrete fracture network when the time equals the 5th year is shown in Fig. 9. The sizes of velocity vectors are proportional to the velocity values, which reflects the permeability of fractures at corresponding points. And the gravity effects are shown in the directions of velocity vectors.

Figs. 10 and 11 make comparisons among different working fluids (water and CO<sub>2</sub>) and discrete fracture networks (parallel-plate and rough-walled) of pressure and temperature distributions. Fig. 10 shows relevant pressure distributions. The comparisons among different discrete fracture networks: Fig. 10-a and c with the working fluid CO<sub>2</sub>, Fig. 10-b and d with the working fluid water, are discussed firstly. In Fig. 10-a and c, it can be found that the pressure distributions for the parallel-plate discrete fracture network has a larger increase just along the fractures in the areas near the left side. In the same area, the pressure distributions for the rough-walled discrete fracture network in the rock matrix and fractures are more uniform. As for Fig. 10-b and d, the phenomenon is not obvious but still observed in the area surrounded by the red border. This can be explained that the rough-walled discrete fracture network model has a higher conductivity compared with the parallel-plate discrete fracture network model. Comparisons among Fig. 10-a and b for the parallel-plate discrete fracture network, Fig. 10-c and d for the rough-walled discrete fracture network are used to analyse the effects of the working fluids. In both parallel-plate and rough-walled discrete networks, it is obvious that CO<sub>2</sub> can lead to the faster increase and decrease of pressure distributions in the areas near the left and right sides separately, which is because the viscosity of CO<sub>2</sub> is much lower than the viscosity of water.

In Fig. 11, the temperature distributions are shown. Similarly, the effects of fracture types (parallel-plate and rough-walled) are investigated through the comparisons among Fig. 11-a and c, Fig. 11-b and d for the same working fluids. It can be also observed that there are larger areas that represents decreasing temperature in Fig. 11-c and d compared with Fig. 11-a and b. This means the heat transfer in the rough-walled discrete fracture network is more efficient for either water or CO<sub>2</sub> as the working fluids. Then, Fig. 11-a and b, Fig. 11-c and d are compared separately. It can be found that the temperature distributions for water as the working fluid have more temperature losses in both parallel-plate and rough-walled discrete fracture networks in areas near the left side due to the fact that the heat capacity of water is higher than that of CO<sub>2</sub>.

In the following section, the variations of stresses and relevant impacting factors during the heat mining process are analysed. As is shown in Fig. 12, there are five sampling locations locating on several fractures, which are used for the study and form a five-spot distribution. In Fig. 13, the permeability of Location #4 is the largest in both parallel-plate and rough-walled discrete fracture networks. Location #3 and #5 have the similar permeabilities for the parallel-plate discrete fracture network in Fig. 13-a. However, the permeability of Location #5 increases much more with time going by and finally is the second largest permeability in Fig. 13-b. And the permeabilities at Location #1 and #2 have the same value by the end of the simulation duration in Fig. 13-a. Unlike in Fig. 13-a, there are small differences of permeability between Location #1 and #2. Fig. 14 shows the normal stress corresponds to the permeability in Fig. 13. It can be found that the normal stress that results in the larger fracturing has a positive correlation with the permeability. The values of normal stress by the time of 30 years follows the sequence: Location #4, #1, #2, #5 and #3 with almost same values

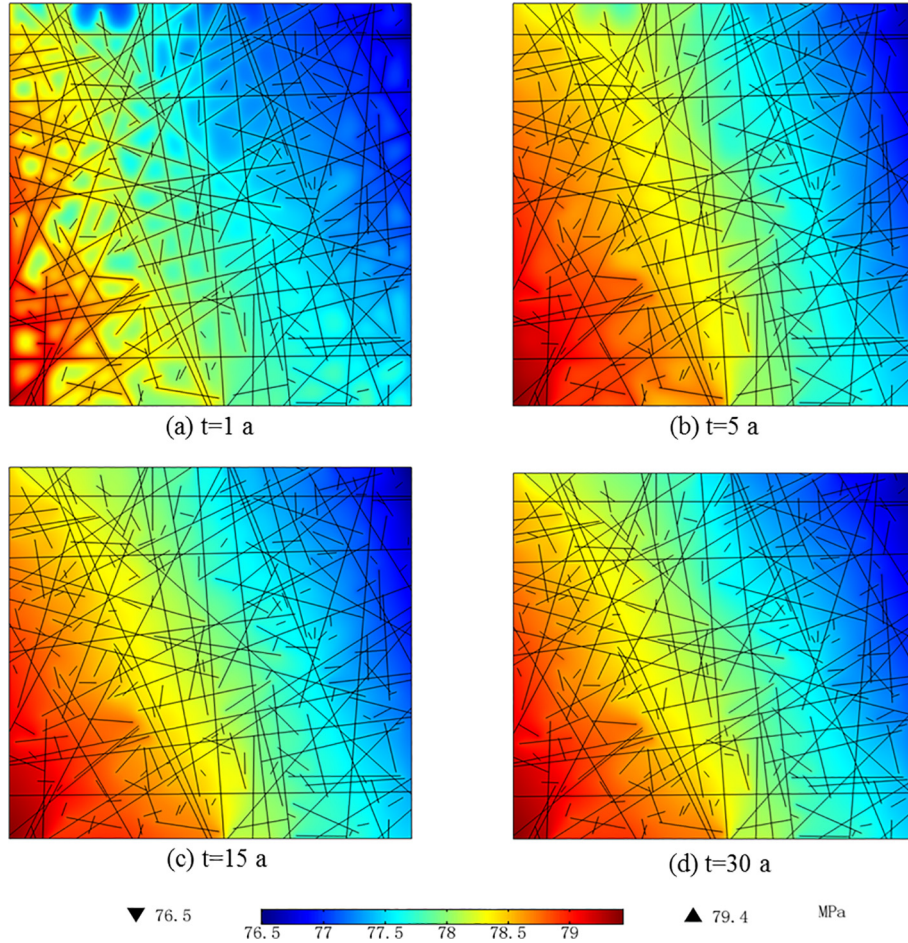


Fig. 7. Pressure distributions with the injection of CO<sub>2</sub> in the rough-walled discrete fracture network.

in both parallel-plate and rough-walled discrete fracture networks.

In this study, the thermal-hydraulic-mechanical (THM) method has been applied for the geothermal reservoir simulation. In order to quantify the effects of temperature on the deformation of the rock matrix and fractures for the five sampling locations, another hydraulic-mechanical (HM) method is adopted to generate the permeability and normal stress for five locations (Figs. 15 and 16). In both Fig. 15-a and b, it is obvious that the permeabilities for Location #3 and #5 have the decreasing trend with the increase of time. As for Location #2 and #4, the permeabilities increase initially and then decrease. As for Location #1, the value of permeability remains constant. This is because the Location #3 and #5 is near the production well that leads to more pressure losses and Location #2 and #4 is near the injection well where pressure increases, which corresponds to Fig. 7. The values of normal stress also present the positive correlations with the values of permeability in Fig. 16 for both parallel-plate and rough-walled discrete fracture networks. In addition, the normal stress curves have similar values in parallel-plate and rough-walled discrete fracture networks. And it should be noticed that the permeability at Location #5 for the rough-walled discrete fracture network in Fig. 15-b always has the second largest value, which is different from the results in Fig. 13-b.

Figs. 17 and 18 play complementary roles in demonstrating the results shown in Figs. 13–16. In Figs. 17 and 18, the permeability and normal stress curves at Location #5 are presented with four cases: (a) parallel-plate DFN for CO<sub>2</sub>; (b) parallel-plate DFN for water; (c) rough-walled DFN for CO<sub>2</sub>; (d) rough-walled DFN for water. Though

different working fluids are applied, it can be found that the generating permeability curves of the rough-walled discrete fracture network locate above the permeability curves of the parallel-plate discrete fracture network for the THM and HM methods in Fig. 17. This phenomenon reflects that the conductivity at Location #5 are better in the rough-walled discrete fracture network. The comparisons of the normal stress are shown in Fig. 18. The values of normal stress for the same working fluid in different settings are almost same with the application of the THM method and similar (pretty small differences) by using the HM method, which are coherent with the observations in Figs. 14 and 16.

The influences of the pressure distributions on the permeability and normal stress at Location #5 are also analysed and summarized. Four different injecting pressures at the depth 6500 m are used for the relevant simulations with the same working fluid CO<sub>2</sub>. In Fig. 18, the relationships between the permeability values and the injecting pressures are positive. And the increases of the permeability in the rough-walled discrete fracture network are larger than the increase in the parallel-plate discrete fracture network. The normal stress curves corresponds to the permeability curves strictly, which imply the normal stress has a positive effect on the permeability increase of the rock matrix and fractures.

On the basis of the results in Figs. 15–20, the impacting parameters (pressure and temperature) on the deformations of the rock matrix and fractures are analysed in details. As for the HM method that does not take temperature into consideration, the decrease of permeability and normal stress with time going by is

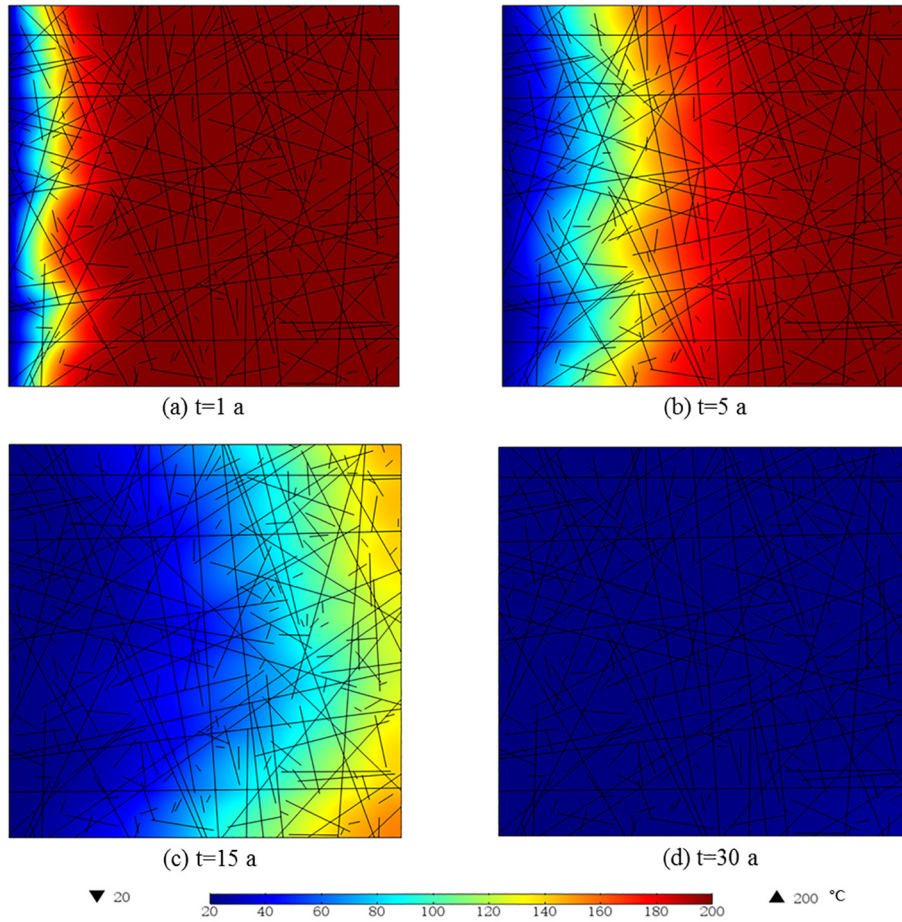


Fig. 8. Temperature distributions with the injection of CO<sub>2</sub> in the rough-walled discrete fracture network.

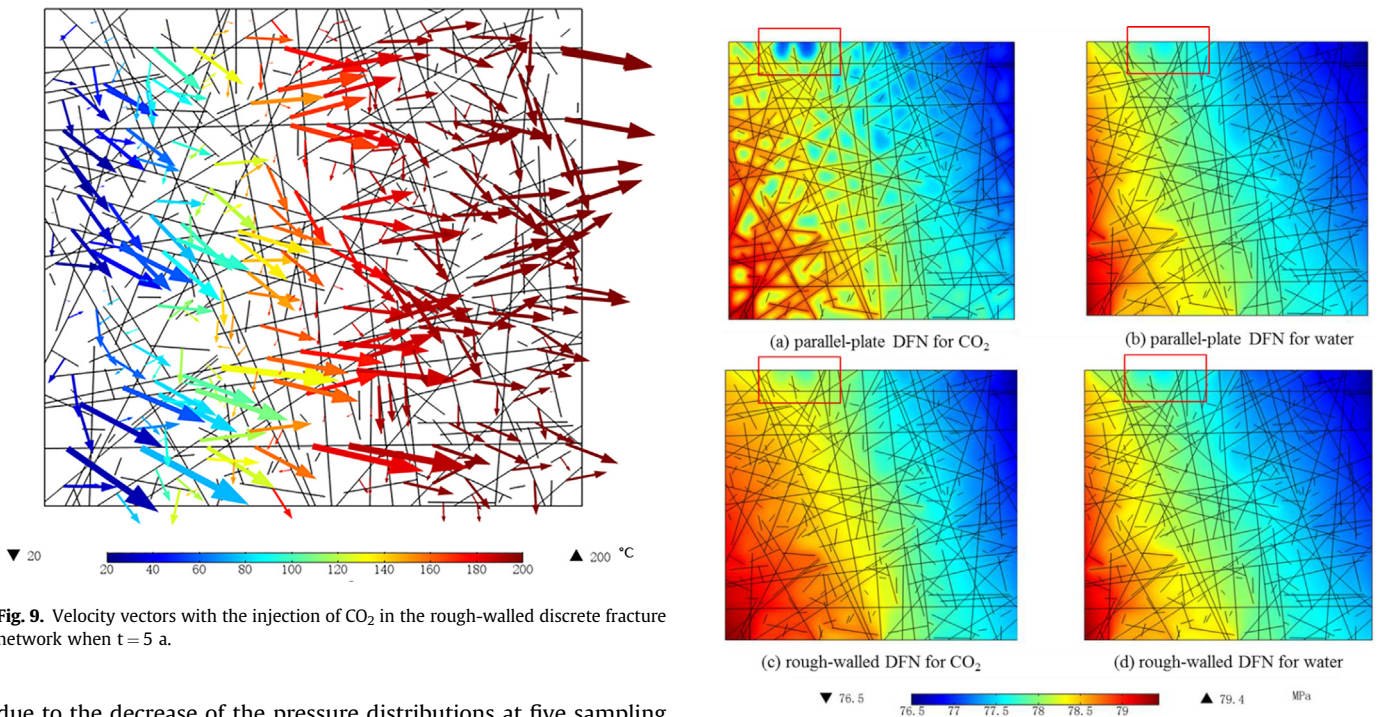


Fig. 9. Velocity vectors with the injection of CO<sub>2</sub> in the rough-walled discrete fracture network when  $t = 5$  a.

Fig. 10. Pressure distributions for water and CO<sub>2</sub> in parallel-plate and rough-walled discrete fracture networks when  $t = 5$  a.

due to the decrease of the pressure distributions at five sampling locations. For example, the permeability and normal stress curves at Location #3 and #5 show constant decreasing trends because

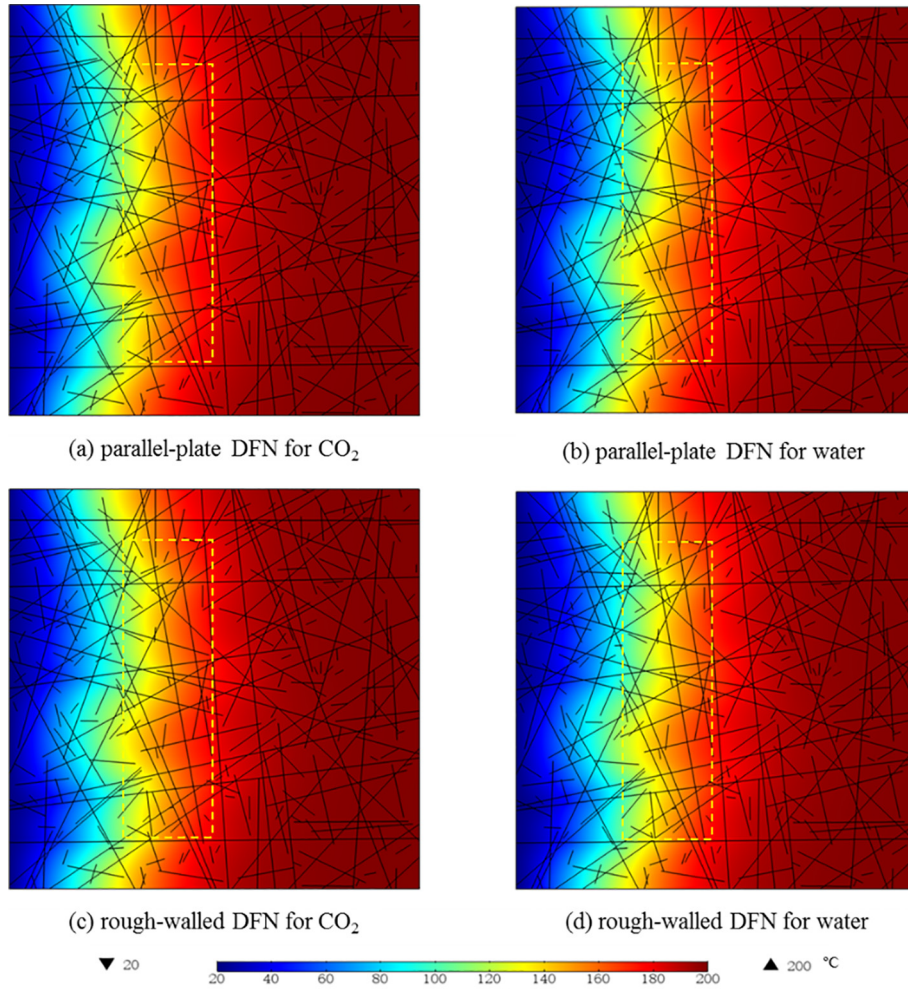


Fig. 11. Temperature distributions for water and CO<sub>2</sub> in parallel-plate and rough-walled discrete fracture networks when  $t = 5$  a.

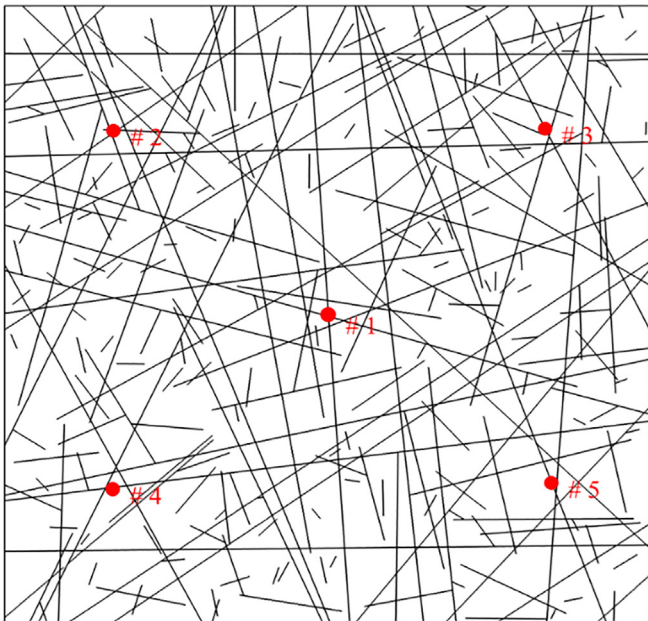


Fig. 12. Spatial locations of five sampling points.

Location #3 and #5 are near the right side (production well), where pressure losses that are induced by production are larger than pressure supply from the injection well in Figs. 15 and 16. The pressure distributions determine the deformations of the rock matrix and fractures when the temperature is not taken into consideration. In addition to the validation that temperature can affect the deformations of the rock matrix and fractures, Fig. 17 shows that the effects of temperature are significant due to the fact that the permeability values with the THM method can reach values up to 10 times higher than those with the HM method. Figs. 19 and 20 give the presentation that the permeability and normal stress increase with the increase in pressure by integrating temperature into model.

Fig. 21 shows the average outlet temperature on the right side corresponds to four cases. At the beginning, the temperature decrease that is induced by water as the working fluid is larger than the temperature decrease that is induced by CO<sub>2</sub>. This is because the temperature decrease is decided by the mass flow rate and heat capacity of water and CO<sub>2</sub> and the heat capacity of water is much larger than that of CO<sub>2</sub>, which leads to a larger temperature decrease of water. With time going by, the temperature decrease of CO<sub>2</sub> becomes larger. In addition, the rough-walled discrete fracture network model leads to a larger temperature decrease compared with the parallel-plate discrete fracture network model, which is determined by the total conductivity that is analysed above.

Unlike decreasing trends of the temperature in Fig. 21, the

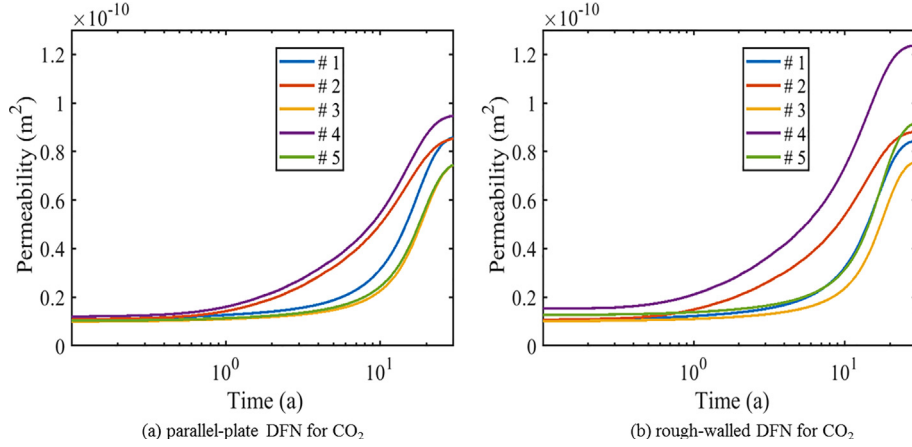


Fig. 13. Corresponding permeability for CO<sub>2</sub> as the working fluid in parallel-plate and rough-walled discrete fracture networks with THM method.

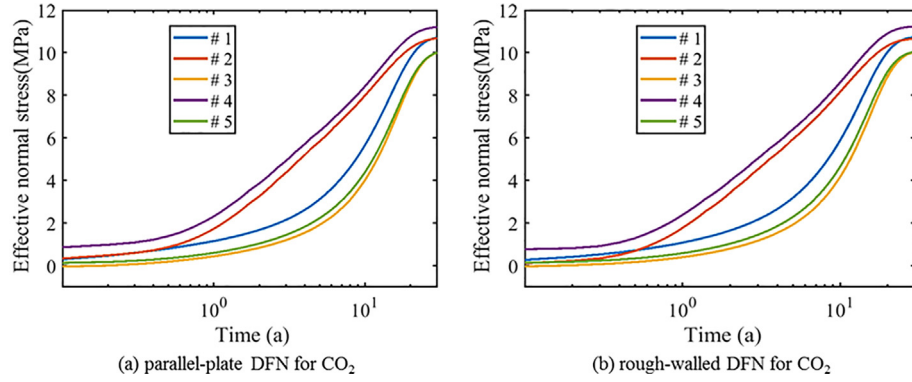


Fig. 14. Corresponding stress for CO<sub>2</sub> as the working fluid in parallel-plate and rough-walled discrete fracture networks with THM method.

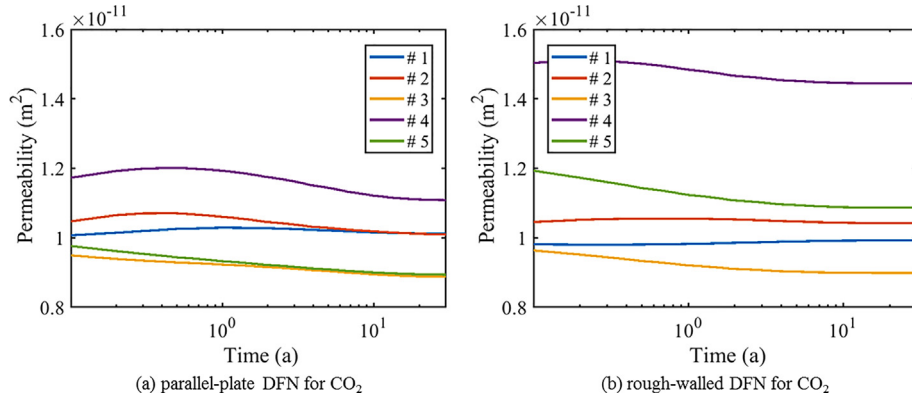


Fig. 15. Corresponding permeability for CO<sub>2</sub> as the working fluid in parallel-plate and rough-walled discrete fracture networks with HM method.

trends of the heat extraction rate for four cases are much more complicated. For all four cases, there is a sharp drop of the heat extraction rate at the beginning, which is due to the elastic potential energy in the reservoir. There are humps appearing on the heat extraction curves in Fig. 22 because of the elastic potential energy.

Fig. 23 presents the heat extraction rate for water and CO<sub>2</sub> as the working fluids without considering the elastic potential energy of the initial reservoir by setting the storage coefficient of the rock matrix and fracture as 0, which is used for comparisons. In addition, the heat extraction rate of water that is much larger than that of

CO<sub>2</sub> at the beginning is due to the initial assumption that the fluid that exists in the reservoir originally is the same as the working fluid. At the same initial reservoir pressure and temperature conditions, the heat capacity of water is about three times to that of CO<sub>2</sub>, which is shown in Fig. 24.

The reservoir temperature is 200°C initially and then decreases with the heat extraction from the reservoir. As is shown in Fig. 24, the heat capacity of CO<sub>2</sub> increases with the decreasing temperature until it reaches a maximum value. Then, it gradually decreases. However, the heat capacity of water decreases along with the decrease of the temperature, reaches a minimum point and then

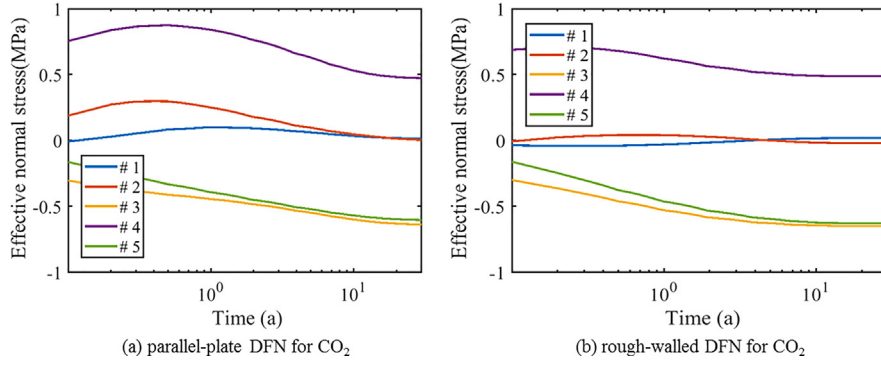


Fig. 16. Corresponding stress for CO<sub>2</sub> as the working fluid in parallel-plate and rough-walled discrete fracture networks with HM method.

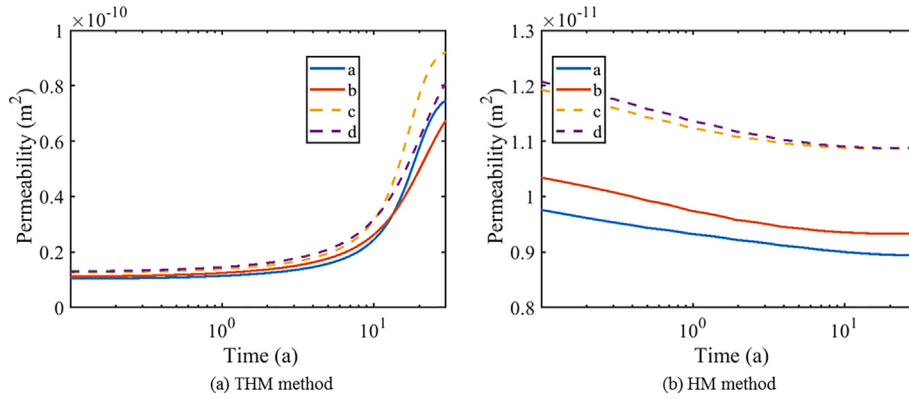


Fig. 17. The permeability at Location #5 for THM and HM method: (a) parallel-plate DFN for CO<sub>2</sub>; (b) parallel-plate DFN for water; (c) rough-walled DFN for CO<sub>2</sub>; (d) rough-walled DFN for water.

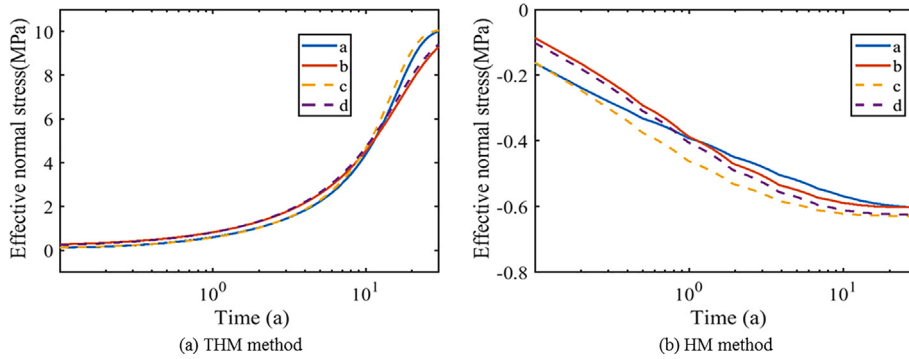


Fig. 18. The stress at Location #5 for THM and HM method: (a) parallel-plate DFN for CO<sub>2</sub>; (b) parallel-plate DFN for water; (c) rough-walled DFN for CO<sub>2</sub>; (d) rough-walled DFN for water.

increases. Though there are initial pressure difference between the reservoir and the production side, the humps on the heat extraction curves of water is induced by the pressure supplement from the injection side. As for CO<sub>2</sub>, the increase of heat capacity and the pressure supplement from the injection side both contribute to corresponding humps on the heat extraction curves.

Figs. 25 and 26 are used to validate the appearance of humps on the heat extraction curves for water and CO<sub>2</sub> respectively. In Fig. 25, it is clear that the humps on the heat extraction curves of water appears earlier with the increase of the injecting pressure on the left side. This is because the pressure supplement from the injection side reaches the production side faster, which reflects that the pressure supplement affects the humps on the heat extraction

curves. In Fig. 26, it is observed that the humps on the heat extraction curves for CO<sub>2</sub> appears earlier the increase of the injecting pressures on the left side. But the appearance of the humps on the heat extraction curves of CO<sub>2</sub> is always later than that of water. This is because in addition to the pressure supplement from the injection side, the heat capacity of CO<sub>2</sub> increases with the heat losses in the reservoir. In Fig. 22, no matter what the working fluid is used, the heat extraction curves for the rough-walled discrete network model locates above those for the parallel-plate discrete fracture network model.

Figs. 27 and 28 are presented to illustrate quantitative comparisons for different working fluids and discrete fracture networks accurately. It is found that the heat extraction rate for CO<sub>2</sub> exceeds

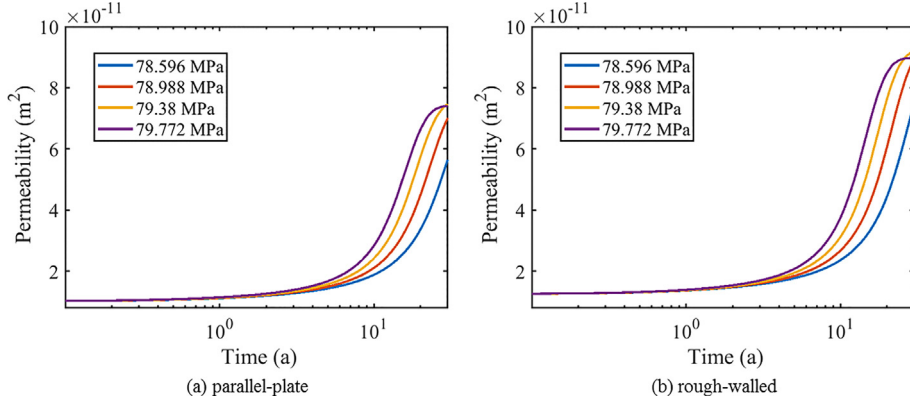


Fig. 19. The permeability at Location #5 for the parallel-plate and rough-walled discrete fracture networks with different injecting pressure boundaries.

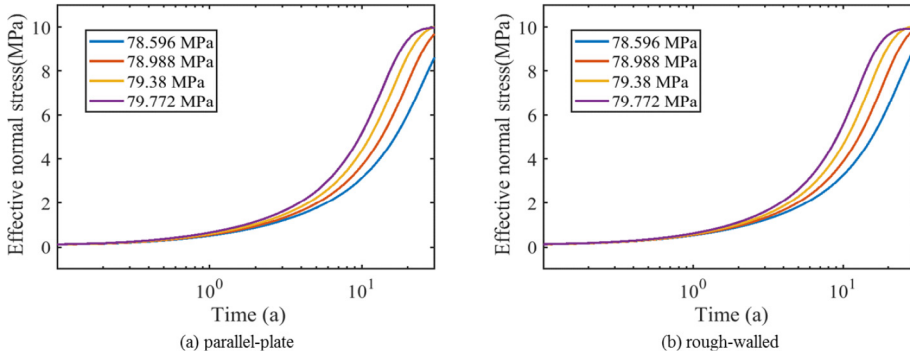


Fig. 20. The stress at Location #5 for the parallel-plate and rough-walled discrete fracture networks with different injecting pressure boundaries.

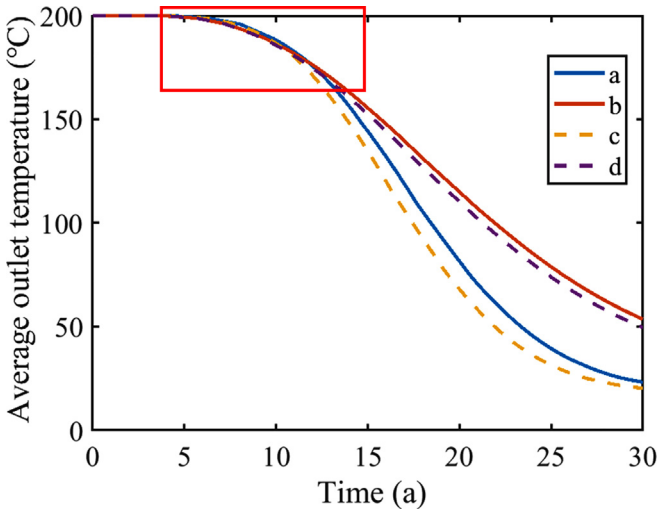


Fig. 21. The relationship between average outlet temperature and time: (a) parallel-plate DFN for CO<sub>2</sub>; (b) parallel-plate DFN for water; (c) rough-walled DFN for CO<sub>2</sub>; (d) rough-walled DFN for water.

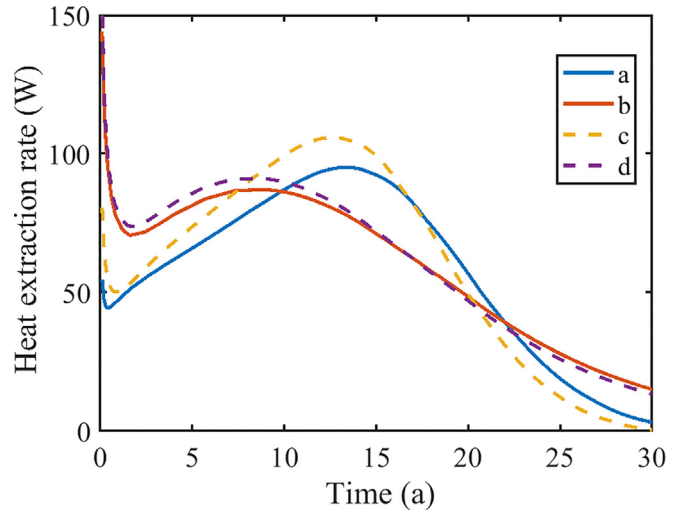


Fig. 22. The relationship between the heat extraction rate and time: (a) parallel-plate DFN for CO<sub>2</sub>; (b) parallel-plate DFN for water; (c) rough-walled DFN for CO<sub>2</sub>; (d) rough-walled DFN for water.

that for water with time going by and then has a sudden drop in Fig. 28. In Fig. 29, there are fluctuations on the ratios of heat extraction rates for CO<sub>2</sub> that are finally parallel to Y axis. The ratios of heat extraction rates for water between the parallel-plate and rough-walled discrete fracture network model show a stable trend. The cumulative heat extraction are shown in Fig. 29. It is observed that after 10–20 years production, the cumulative heat extractions for CO<sub>2</sub> as the working fluid in both parallel-plate and rough-walled

discrete fracture networks exceed those for water, which means water is a more efficient working fluids in 10–20 years since the EGS begins to work.

## 6. Conclusions

In this study, the properties of single rough fracture have been

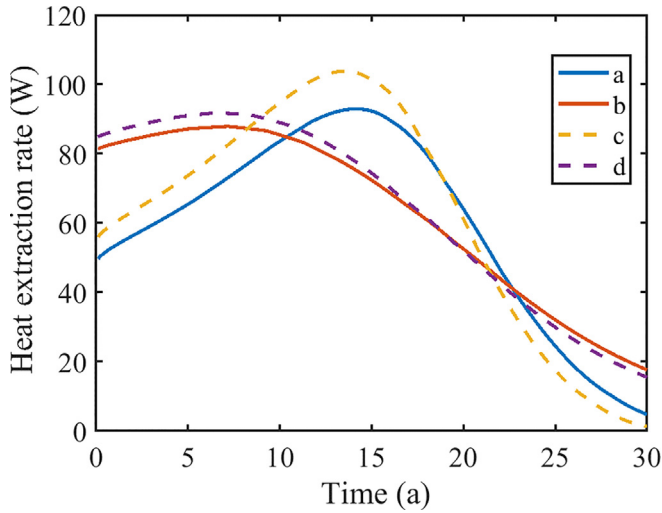


**Fig. 23.** The relationship between the heat extraction rate and time without considering the elastic potential energy: (a) parallel-plate DFN for CO<sub>2</sub>; (b) parallel-plate DFN for water; (c) rough-walled DFN for CO<sub>2</sub>; (d) rough-walled DFN for water.

characterized and the rough-walled discrete fracture network model has been successfully developed by integrating the thermal-hydraulic-mechanical (THM) coupling process. The mass and heat transfer and mechanical process in the reservoir with the injection of water and CO<sub>2</sub> respectively were simulated by the new model.

On the basis of the simulation results, it is found that the pressure and temperature distributions of rough-walled discrete fracture network model are more complicated than those of the parallel-plate discrete fracture network model. The rough-walled discrete fracture network model in this study presents higher

conductivities than the parallel-plate discrete fracture network, which have direct effects on the mass and heat transfer. This is because the aperture heterogeneities of the rough-walled fractures affect interconnections among fractures and consequently the effective permeability of the whole fracture network. Sensitivity analysis shows that the permeability of the rock matrix and fractures are affected by the pressure and temperature distributions, which has a positive correlation with corresponding normal stress. It is also found that the permeability of the rough-walled fractures is higher than the permeability of the parallel-plate fractures when the normal stresses are same or similar and the differences become larger with the increase of the normal stresses by investigating five sampling locations.

A detailed evaluation has been made to investigate heat extraction rates from the geothermal reservoir. Corresponding to the statements above, the rough-walled discrete fracture network model has higher production rates compared with the parallel-plate discrete fracture network model. With considering the heat capacity that changes with temperature, there are humps (maximum heat rates) on the curves of heat extraction rate due to the comprehensive functions of temperature range and heat capacity. Although the average outlet temperature for CO<sub>2</sub> as the working fluid drops faster than that for water, the heat capacity of water is larger than the heat capacity of CO<sub>2</sub>. As a result, the heat production rate for water as the working fluid is larger than that of CO<sub>2</sub> initially and exceeded by that of CO<sub>2</sub> with continuing productions. Furthermore, water as the working fluid has a larger heat extraction accumulation about 20 years. It can be concluded that the heat extraction efficiency of water as the working fluids is better, at least not less than that CO<sub>2</sub> for certain durations in some cases.

The parallel-plate discrete fracture network model plays a role in validating the rough-walled discrete fracture network model. This study proposes a new model for the EGS simulation, which is

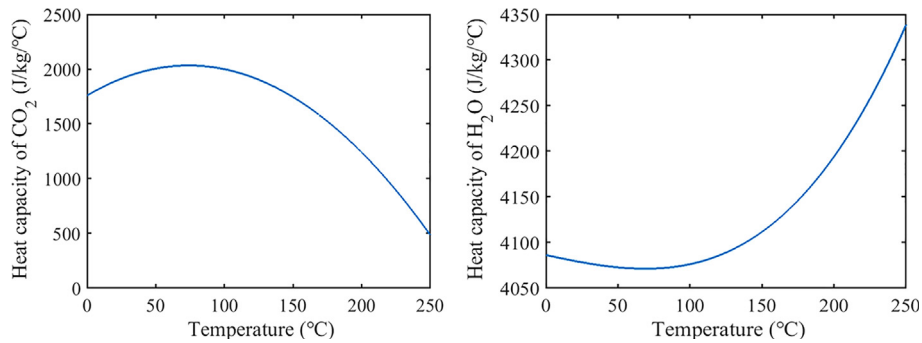


**Fig. 24.** The relationship between heat capacity and temperature.

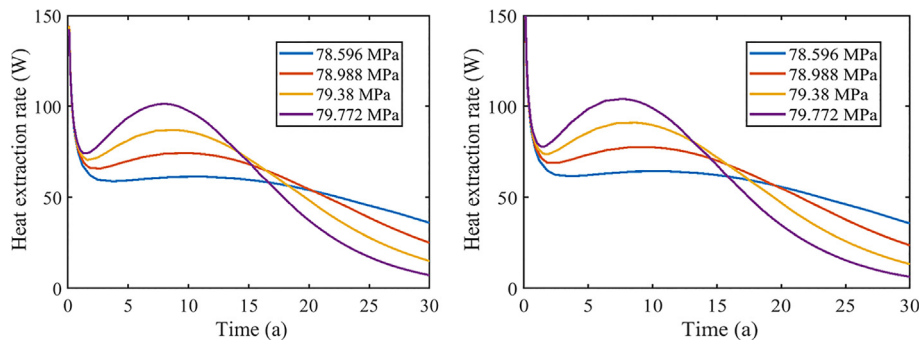


**Fig. 25.** The relationship between heat extraction rate and time for water with different injecting pressures.

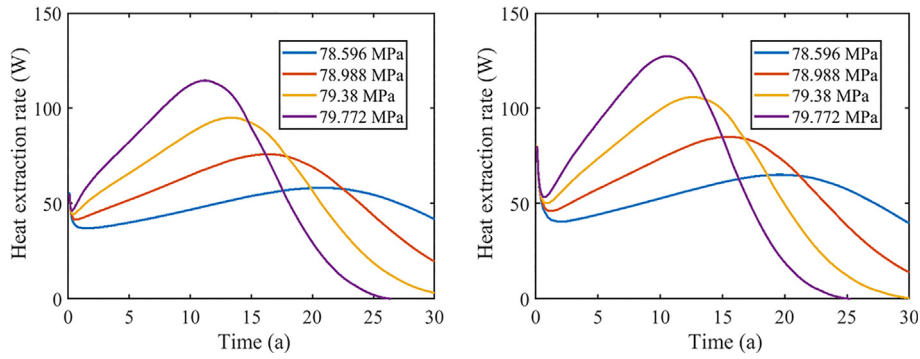


Fig. 26. The relationship between heat extraction rate and time for CO<sub>2</sub> with different injecting pressures.

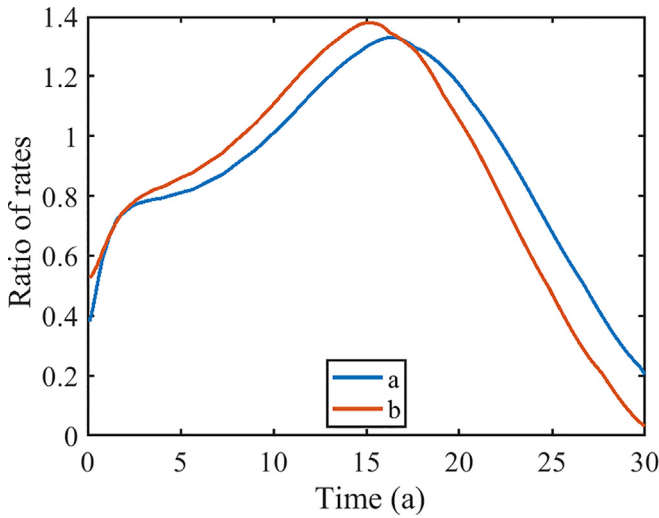


Fig. 27. Ratios of rates for CO<sub>2</sub>; H<sub>2</sub>O: (a) parallel-plate; (b) rough-walled.

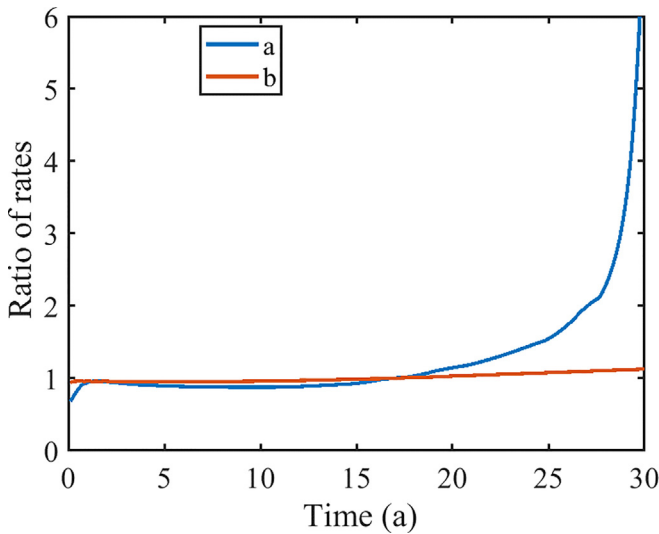


Fig. 28. Ratios of rates for parallel-plate: rough-walled: (a) CO<sub>2</sub>; (b) H<sub>2</sub>O.

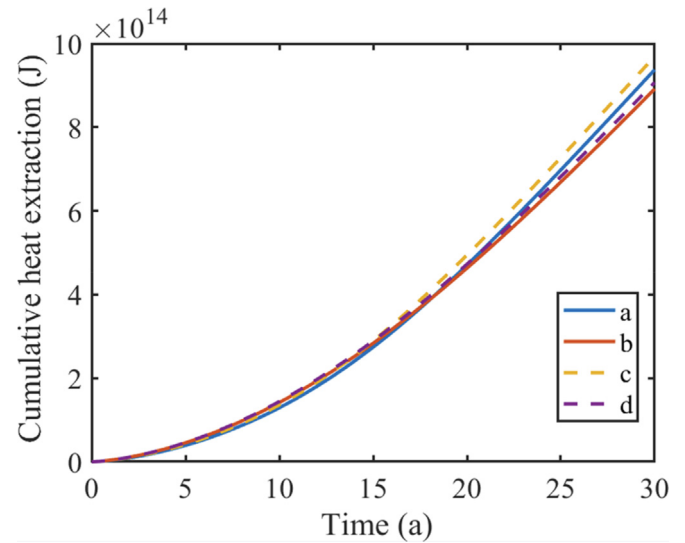


Fig. 29. Cumulative heat extraction: (a) parallel-plate DFN for CO<sub>2</sub>; (b) parallel-plate DFN for water; (c) rough-walled DFN for CO<sub>2</sub>; (d) rough-walled DFN for water.

further study.

### Acknowledgement

This study was jointly supported by the National Natural Science Foundation of China (Grant NO.51774317).

### References

- [1] William EG. Geothermal energy: renewable energy and the environment. CRC Press; 2010.
- [2] Johnston IW, Narsillo GA, Colls S. Emerging geothermal energy technologies. *KSCE J Civil Eng* 2011;15(4):643–53.
- [3] Omar E, Haitham AR, Frede B. Renewable energy resources: current status, future prospects and their enabling technology. *Renew Sustain Energy Rev* 2014;39:748–64.
- [4] BP plc. BP 2017 statistical review of world energy. June 2018.
- [5] Geothermal Energy Association. Annual U.S. & global geothermal power production report. 2016. 2016. Washington, D.C.
- [6] Brown DW, Duchane DV, Heiken G, Heiscu VT. Mining the earth's heat: Hot Dry rock geothermal energy. Springer Science & Business Media; 2012.
- [7] Tester JW, Anderson BJ, Batchelor AS, Blackwell DD, et al. The future of geothermal energy, Impact of Enhanced Geothermal Systems on the United States in the 21<sup>st</sup> century. report. MIT; 2006.
- [8] Xu RN, Zhang L, Zhang FZ, Jiang PX. A Review on heat transfer and energy conversion in the enhanced geothermal systems with water/CO<sub>2</sub> as working fluid. *Int J Energy Res* 2015;39(13):1722–41.
- [9] Pruess K. Enhanced geothermal systems (EGS) using CO<sub>2</sub> as working fluid – a novel approach for generating renewable energy with simultaneous sequestration of carbon. *Geothermics* 2006;35:351–67.

of great help for the optimization of EGS production efficiency and a solid foundation for further research in the geothermal reservoir characterization and simulation. The effects of different discrete fracture networks and relevant parameters will be investigated in

- [10] Zhu JL, Hu KY, Lu XL, Huang XX, Liu KT, Wu XJ. A review of geothermal energy resources, development, and applications in China: current status and prospects. *Energy* 2015;93:466–83.
- [11] Olasolo P, Juárez MC, Morales MP, Sebastiano DA, Liarte IA. Enhanced geothermal systems (EGS): a review. *Renew Sustain Energy Rev* 2016;56:133–44.
- [12] Moeck IS. Catalog of geothermal play types based on geologic controls. *Renew Sustain Energy Rev* 2014;37:867–82.
- [13] Shaik AR, Rahman SS, Tran NH, Tran T. Numerical simulation of fluid–rock coupling heat transfer in naturally fractured geothermal system. *Appl Therm Eng* 2011;31:1600–6.
- [14] Borgia A, Pruess K, Kneafsey TJ, Oldenburg CM, Pan I. Numerical simulation of salt precipitation in a fractured CO<sub>2</sub>-Enhanced geothermal system. *Geothermics* 2012;44:13–22.
- [15] Juliusson E, Horne RN. Optimization of injection scheduling in fractured geothermal reservoirs. *Geothermics* 2013;48:80–92.
- [16] Zhang FZ, Jiang PX, Xu RN. System thermodynamic performance comparison of CO<sub>2</sub>-EGS and water-EGS systems. *Appl Therm Eng* 2013;61:236–44.
- [17] Luo F, Xu RN, Jiang PX. Numerical investigation of fluid flow and heat transfer in a doublet enhanced geothermal system with CO<sub>2</sub> as the working fluid (CO<sub>2</sub>-EGS). *Energy* 2014;64:307–22.
- [18] Borgia A, Oldenburg CM, Zhang R, Pan LH, Daley TM, Finsterle S, Ramakrishnan TS. Simulations of CO<sub>2</sub> injection into fractures and faults for improving their geophysical characterization at EGS sites. *Geothermics* 2017;69:189–201.
- [19] Jiang F, Chen J, Huang W, Luo L. A three-dimensional transient model for EGS subsurface thermo-hydraulic process. *Energy* 2014;72:300–10.
- [20] Fox DB, Koch DL, Tester JW. An analytical thermos hydraulic model for discretely fractured geothermal reservoirs. *Water Resour Res* 2016;52(9):6792–817.
- [21] Sun Z, Zhang X, Xu Y, Yao J, Wang H, Lv S, Sun Z, Huang Y, Cai M, Huang X. Numerical simulation of the heat extraction in EGS with thermal-hydraulic-mechanical coupling method based on discrete fractures model. *Energy* 2017;120:20–33.
- [22] Borgia A, Oldenburg CM, Zhang R, Pan L, Daley TM, Finsterle S, Ramakrishnan TS. Simulating CO<sub>2</sub> injection into fractures and faults for improved characterization of EGS sites. *Geothermics* 2017;69:189–201.
- [23] Huang WB, Cao WJ, Jiang FM. Heat extraction performance of EGS with heterogeneous reservoir: a numerical evaluation. *Int J Heat Mass Transf* 2017;108:645–57.
- [24] Asai P, Panja P, Velasco R, Mclellan J, Moore J. Fluid flow distribution in fractures for a doublet system in Enhanced Geothermal Systems (EGS). *Geothermics* 2018;75:171–9.
- [25] Lomize GM. Flow in fractured rocks (in Russian). Moscow, Russia: Gessmergoizdat; 1951.
- [26] Andersson J, Dverstorp B. Conditional simulations of fluid flow in three-dimensional networks of discrete fractures. *Water Resour Res* 1986;23(10):1876–86.
- [27] Berkowitz B, Braester C. Solute transport in fracture channel and parallel plate models. *Geophys Res Lett* 1991;18(2):227–30.
- [28] Bruderer-Weng C, Cowie P, Bernabe Y, Main I. Relating flow channelling to tracer dispersion in heterogeneous networks. *Adv Water Resour* 2004;27:843–55.
- [29] Wang M, Chen Y, Ma G, Zhou J, Zhou C. Influence of surface roughness on nonlinear flow behaviors in 3D self-affine rough fractures: Lattice Boltzmann simulations. *Adv Water Resour* 2016;96:373–88.
- [30] Dou Z, Zhou Z, Sleep BE. Influence of wettability on interfacial area during immiscible liquid invasion into a 3D self-affine rough fracture: Lattice Boltzmann simulations. *Adv Water Resour* 2013;61:1–11.
- [31] Zou LC, Jing LR, Cvetkovic V. Modeling of flow and mixing in 3D rough-walled rock fracture intersections. *Adv Water Resour* 2017;107:1–9.
- [32] Dreuzy JR, Meheust Y, Pichot G. Influence of fracture scale heterogeneity on the flow properties of three-dimensional discrete fracture networks (DFN). *J Geophys Res* 2012;117:B11207.
- [33] Jing Y, Armstrong RT, Mostaghimi P. Rough-walled discrete fracture network modelling for coal characterisation. *Fuel* 2016;191:442–53.
- [34] Chen Y, Ma GW, Wang HD. Heat extraction mechanism in a geothermal reservoir with rough-walled fracture networks. *Int J Heat Mass Transf* 2018;126:1083–93.
- [35] Feng ZJ, Zhao YS, Zhou AC, Zhang N. Development program of hot dry rock geothermal resource in the Yangbajing Basin of China. *Renew Energy* 2012;39(1):490–5.
- [36] Zeng YC, Wu NY, Su Z, Wang XY, Hu J. Numerical simulation of heat production potential from hot dry rock by water circulating through a novel single vertical fracture at Desert Peak geothermal field. *Energy* 2013;63:268–82.
- [37] Yao J, Zhang X, Sun ZX, Huang ZQ, Liu JR, Li Y, Xin Y, Yan X, Liu WZ. Numerical simulation of the heat extraction in 3D-EGS with thermal-hydraulic-mechanical coupling method based on discrete fractures model. *Geothermics* 2018;74:19–34.
- [38] Huang SL, Oelfke SM, Speke RC. Applicability of fractal characterization and modelling to rock joint profiles. *Int J Rock Mech Min Sci Geomech Abstr* 1992;29(2):89–98.
- [39] Schmittbuhl J, Steyer A, Jouniaux L, Toussaint R. Fracture morphology and viscous transport. *Int J Rock Mech Min Sci* 2008;45(3):422–30.
- [40] Develi K, Babadagli T. Quantification of natural fracture surfaces using fractal geometry. *Math Geol* 1998;30(8):971–98.
- [41] Lei QH, Wang XG, Xiang JS, Latham J. Polyaxial stress-dependent permeability of a three-dimensional fractured rock layer. *Hydrogeol J* 2017;8:2251–62.
- [42] Saeid S, Al-Khoury R, Barends F. An efficient computational model for deep low-enthalpy geothermal systems. *Comput Geosci* 2013;51:400–9.
- [43] Chen BG, Song EX, Cheng XH. A numerical method for discrete fracture network model for flow and heat transfer in two-dimensional fractured rocks. *Chin J Rock Mech Eng* 2014;33(1):43–51 [in Chinese].
- [44] Xu C, Dowd PA, Zhao FT. A simplified coupled hydro-thermal model for enhanced geothermal systems. *Appl Energy* 2015;140:135–45.
- [45] Zhao YS, Feng Z, Yang D, Liang W. Thermo-hydro-mechanical coupled mathematical model of fractured media and numerical simulation of a 3D enhanced geothermal system at 573 K and buried depth 6000 – 7000 m. *Energy* 2015;82:193–205.
- [46] Wu C. Hydraulic. second ed. Beijing: Higher Education Press; 1983 [in Chinese].
- [47] CMG Winprop tutorial 2015.
- [48] Cui GD, Zhang L, Ren B, Enechukwu C, Liu YM, Ren SR. Geothermal exploitation from depleted high temperature gas reservoirs via recycling supercritical CO<sub>2</sub>: heat mining rate and salt precipitation effects. *Appl Energy* 2016;183:837–52.
- [49] National Institute of Standards and Technology. NIST reference fluid thermodynamic and transport properties database (REFPROP). Version 9.0. 2011.
- [50] Randolph JB. Coupling geothermal energy capture with carbon dioxide sequestration in naturally permeable, porous geologic formations - a novel approach for expanding geothermal energy utilization. University of Minnesota Digital Conservancy; 2011.